# A Fourier-Based Method for the Distribution of Breaking Crests from Video Observations

JIM THOMSON AND ANDREW T. JESSUP

*Applied Physics Laboratory, University of Washington, Seattle, Washington*

(Manuscript received 31 January 2008, in final form 2 February 2009)

ABSTRACT

A Fourier-based method is presented to process video observations of water waves and calculate the speed distribution of breaking crest lengths. The method has increased efficiency and robust statistics compared with conventional algorithms that assemble distributions from tracking individual crests in the time domain. The method is tested using field observations (video images of whitecaps) of fetch-limited breaking waves during case studies with low (6.7 m $s^{-1}$), moderate (8.5 m $s^{-1}$), and high (12.6 m $s^{-1}$) wind speeds. The method gives distributions consistent with conventional algorithms, including breaking rates that are consistent with direct observations. Results are applied to obtain remote estimates of the energy dissipation associated with wave breaking.

## 1. Introduction

Wave breaking at the ocean surface is a primary mechanism for exchange between the ocean and the atmosphere, and a thorough understanding of this process is needed for accurate modeling of climate change, pollutant transport, and ship safety. The breaking of deep-water surface waves remains a poorly quantified process (Banner and Peregrine 1993; Melville 1996), in part because direct field observations are difficult and costly (Gemmrich and Farmer 1999, 2004). With the advent of digital video recording, remote observations are becoming more common and are a promising area of research.

For remote quantification of breaking waves, a key quantity of interest is the normalized distribution of total breaking crest lengths per unit area as a function of speed $\Lambda(c)$, which was introduced by Phillips (1985). By definition, the average total length of breaking crests per unit area is

$$L_{\text{total}} \equiv \int \Lambda(c)dc, \tag{1}$$

where $c$ is speed and $dc$ is the speed bandwidth used to normalize the distribution. The moments of $\Lambda(c)$ can be related directly to kinematic quantities (breaking rates; see section 5b), and indirectly to dynamic quantities (energy dissipation; see section 5c) using a numerical constant $b$ (Duncan 1981).

Recent estimates of $\Lambda(c)$ have used video crest tracking algorithms (Gemmrich et al. 2008), video particle image velocimetry (PIV; Melville and Matusov 2002), infrared crest tracking combined with PIV (Jessup and Phadnis 2005), and high-resolution radar backscatter (Phillips et al. 2001). Generally, breaking crests are found to be broadly distributed at speeds somewhat less than the linear phase speeds, consistent with laboratory measurements (Banner and Pierson 2007; Rapp and Melville 1990; Melville and Rapp 1985), and large-scale crests are found to dominate the dynamics.

Although the recent estimates of $\Lambda(c)$ represent substantial progress toward remote quantification of breaking waves, there are noteworthy uncertainties in each of the methods. Phillips et al. (2001) determine crest speeds, but lack direct estimates of crest lengths owing to limitations in their radar backscatter observations. Melville and Matusov (2002) determine both crest speeds and lengths, but only observe crests instantaneously owing to the short dwell time of their airborne observations. In addition, Melville and Matusov (2002) find breaking rates that are inconsistent with measured wind speeds. Gemmrich et al. (2008) obtain

*Corresponding author address:* Jim Thomson, Applied Physics Laboratory, University of Washington, 1013 NE 40th St., Seattle, WA 98105.
E-mail: jthomson@apl.washington.edu

DOI: 10.1175/2009JTECHO622.1

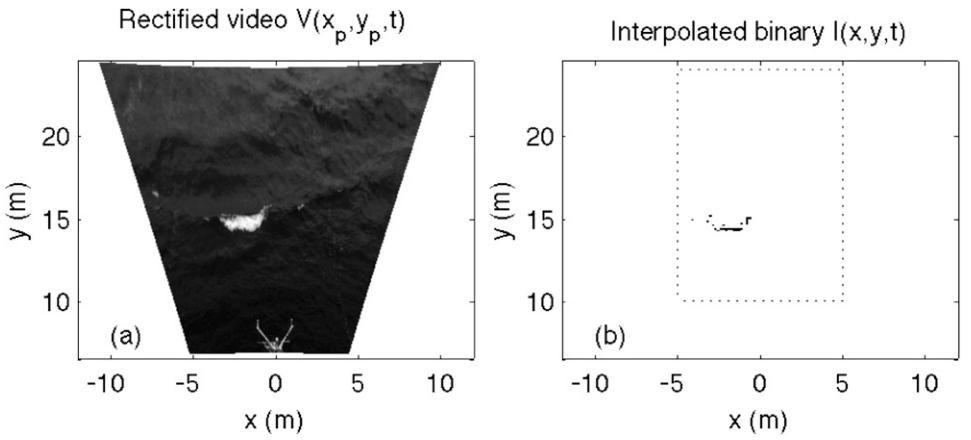


FIG. 1. Example showing (a) the video data and (b) the extracted binary of a breaking crest ($x = -2$ m, $y = 15$ m) during moderate wind conditions (case 2, 8.5 m s$^{-1}$). (a) Video frames are corrected for lens distortion and perspective, resulting in a trapezoidal field of view that is approximately 10 m $\times$ 15 m. (b) Binary images are interpolated to a uniform grid (dotted box) for spectral processing after thresholding and differencing to find the leading edge. There is an instrument frame in the lower portion of the image ($-1 < x < 1$, $8 < y < 9$), the video camera is located at the origin ($x = 0$, $y = 0$), and the $y$ axis is aligned with 164°T.

consistent breaking rates using video observations from a stable platform [research platform (R/P) FLIP]; however, results are sensitive to the choice of a characteristic speed for each crest. Similarly, Jessup and Phadnis (2005) obtain consistent breaking rates in a laboratory experiment, but $\Lambda(c)$ distributions are sensitive to the choice of PIV algorithm. Finally, values of $b$ (necessary to calculate dynamic quantities) vary by two orders of magnitude, from $10^{-4}$ (Phillips et al. 2001) to $10^{-2}$ (Melville and Matusov 2002).

There is an ongoing debate in the literature concerning the physical interpretation of $\Lambda(c)$, based in part on the measurement techniques employed. Gemmrich et al. (2008) assign a characteristic speed and length to each breaking crest, in line with the original formulation (Phillips 1985; Duncan 1981). In contrast, Melville and Matusov (2002) assign instantaneous speeds to fragments of crests, such that speed variations are included, but individual crests are divided into dissociated segments. Here, we present a hybrid interpretation that captures the instantaneous speeds and retains each crest as a distinct contribution. Restated, we consider a distribution of speed and length for each breaking event and then define $\Lambda(c)$ as the average of these components over all events. The approach describes both the evolution of an individual breaker, as well the episodic nature of the events contributing to the average distribution. This requires that breaking crests remain in the camera field of view for their full duration (or be appropriately windowed and tapered; see section 3b), which is not possible using airborne data (Melville and Matusov 2002), or when the field of view is smaller than the largest waves (Gemmrich et al. 2008).

In the following sections, field observations of deep-water wave breaking (section 2) are used to determine $\Lambda(c)$ with a Fourier-based method (section 3), after which the results are validated with two time-domain methods (section 4). A case study with moderate wind speed is used to demonstrate the methods, and then additional field observations are presented and moments of $\Lambda(c)$ are evaluated (section 5). Finally, physical interpretation of the various methods and resulting distributions is discussed (section 6).

## 2. Field observations

Video observations of breaking surface waves (e.g., the whitecap in Fig. 1) were collected at the north end of Lake Washington in Washington state (47°44.542′N, 122°16.518′ W) in 11.5-m water depth from a 10-m high tower aboard the R/V *Henderson* (Applied Physics Laboratory, University of Washington). The fetch is approximately 7 km long, spanning from Sand Point to Kenmore, and the resulting waves are fetch-limited and nearly unidirectional, as observed in previous studies on the lake (Weisman et al. 1984).

During a 24-h period spanning 14–15 November 2006, conditions evolved from flat calm to rough seas with the onset of strong southerly (mean direction 164° T) winds. From this period, three 30-min-long case studies were selected to demonstrate the $\Lambda(c)$ method. The case study conditions are described in Table 1, using the

TABLE 1. Wind and wave conditions during the three cases studies. Wave period refers to the peak in altimeter spectra; wavelength and phase speed $c_p$ are determined from the linear deep-water limit at the peak period.

| | Case 1 | Case 2 | Case 3 |
|---|---|---|---|
| Wind speed (m $s^{-1}$) | 6.7 | 8.5 | 12.5 |
| Wind gust (m $s^{-1}$) | 9.0 | 11.0 | 16.5 |
| Wave height (cm) | 10 | 22 | 38 |
| Wave period (s) | 1.7 | 2.4 | 2.7 |
| Wavelength (m) | 4.6 | 9.2 | 12.0 |
| Wave age ($c_p/U_{10}$) | 0.40 | 0.45 | 0.35 |
| Wave steepness ($H_s/\lambda_p$) | 0.022 | 0.024 | 0.032 |
| Frequency of breaking ($h^{-1}$) | 19 | 27 | 40 |

wind speed from a propeller anemometer (R.M. Young Model 05701) and the wave height from an ultrasonic altimeter (Siemens Milltronics AiRanger DPL). The wave age, defined as the ratio of the dominant phase speed $c_p$ to the 10-m wind speed $U_{10}$, remained less than 1 throughout this period, indicating highly forced breaking waves. The wave steepness, defined as the ratio of significant wave height $H_s$ to dominant wavelength $\lambda_p$, increased with breaker activity, consistent with previous work (Banner et al. 2000). The dominant phase speed and wavelength are determined using the linear deep-water limit at the peak in the altimeter spectra.

Video data (1024 × 768 pixels) were collected at 20 Hz and later subsampled to 10 Hz ($dt = 0.1$ s) from an eight-bit grayscale firewire camera (Point Gray Research Flea). Using a lens with 45° horizontal field of view orientated at 50° incidence angle, the imaged area is approximately 15 m on a side (see Fig. 1) with a pixel resolution of $O(1\text{ cm})$. Interpolation to uniform spacing for spectral processing (section 3b) reduced the resolution to $dx = 15$ cm and $dy = 11$ cm. Additional instrumentation included an infrared camera/laser system and acoustic current profilers (to be presented in a future paper).

## 3. Fourier component method

The method for calculating $\Lambda(c)$ transforms a standard Fourier frequency–wavenumber representation to a speed spectrum weighted by breaking pixels in a video time series (Fig. 1). Similar transforms have been used successfully to determine the mean speeds of nearshore currents (Chickadel et al. 2003) and of fibrillation signals in the heart (Bayly et al. 1994). We extend the analysis beyond evaluation of the mean and examine the full spectrum of speed, which is then renormalized to estimate $\Lambda(c)$. Compared with an equivalent time-domain approach, the method is computationally efficient, robust, and objective.

### a. Conversion to binary images

First, the digital video data $V$ are rectified (corrected for camera perspective) and undistorted (corrected for camera lens) to determine the real-world coordinates $x_p$, $y_p$ for each pixel (Holland et al. 1997), as shown in Fig. 1. The choice of a local coordinate system is arbitrary, and alignment of the $y$ axis along the mean wave direction is used to simplify both presentation and computation. Although constant at $\hat{y} = 164°$T for these data, this local coordinate system can be rotated as conditions change, such that the subsequent analysis retains a useful principle axis.

Next, neighboring images (at time $t$ and separation $dt = 0.1$ s) are subtracted to emphasize the leading edges of breaking crests (Gemmrich et al. 2008),

$$\Delta V(x_p, y_p, t) = V(x_p, y_p, t + dt) - V(x_p, y_p, t), \quad (2)$$

which appear as bright whitecaps moving through the camera field of view. Then, the differenced images (still separated by $dt$) are converted to a binary images (1 = breaker pixel, 0 = background pixel) by

$$I(x_p, y_p, t) = \begin{cases} 1 & \text{for } \Delta V(x_p, y_p, t) > n\sigma_V + \overline{V} \\ 0 & \text{for } \Delta V(x_p, y_p, t) < n\sigma_V + \overline{V} \end{cases}, \quad (3)$$

where $\sigma_V$ and $\overline{V}$ indicate the time–space standard deviation and mean, respectively, of the video signal and $n$ is a tunable sensitivity parameter. This first-derivative threshold was manually confirmed to identify breaking crests (i.e., whitecaps) while excluding sun glitter, windrows, and other visual noise. The nonbreaking features are excluded because they are nearly stationary at fast time scales ($dt = 0.1$ s). Thresholding ensures that only actively breaking crests contribute to $\Lambda(c)$; however, whitecap pixels are sufficiently bright (often saturating the camera detector) that the results are similar over the range $n = 1$ to $n = 3$. For the data presented here, $n = 1$ is used throughout, because it produces the best overall agreement between the first moment of $\Lambda(c)$ and a direct calculation of the breaking rate (section 5b). Results are also similar without subsampling from 20 to 10 Hz, indicating that the fastest crests observed (~4 m $s^{-1}$) are not aliased.

### b. Frequency–wavenumber spectra

Prior to taking the fast Fourier transform, each of the $N$ binary images is interpolated from real-world pixel coordinates (trapezoidal 1024 × 768 point grid of $x_p$, $y_p$)

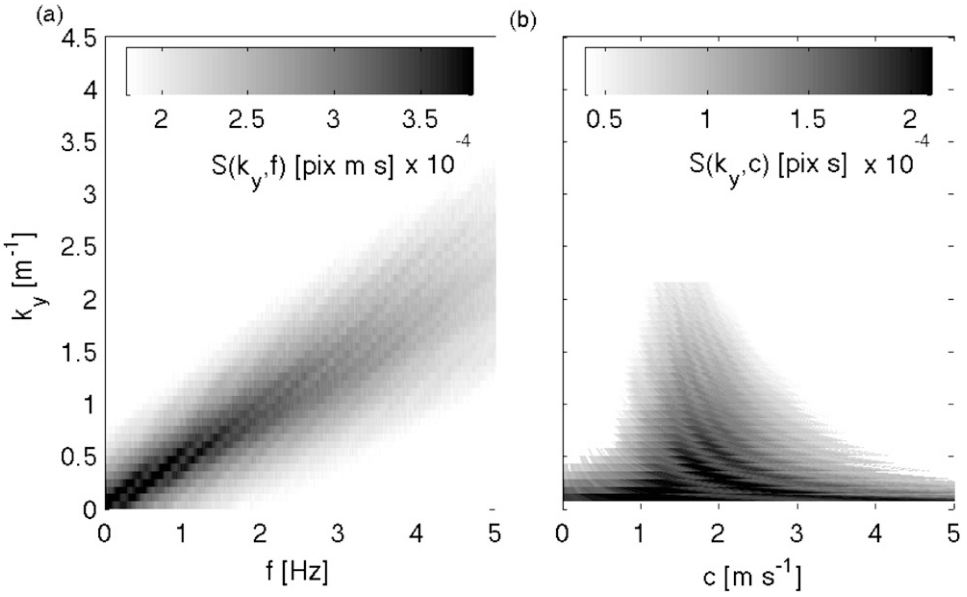


FIG. 2. Example amplitude spectral density $S$ as a function of (a) wavenumber and observed frequency and (b) wavenumber and speed. Spectra are ensemble averaged from video data during case 2 (moderate wind strength at 8.5 m $s^{-1}$), and spectra from other cases have similar concentrations around $c = f/k_y$ slopes. The video data have been processed to retain only the breaking crests, and the window length is short (102 s) to isolate the motion of breaking crests; without these steps, the spectra would include a dispersion curve caused by propagating waves and whitening caused by intermittent breaking.

to uniform coordinates (rectangular $64 \times 128$ point grid of $x$, $y$) with resolution $dx = 15$ and $dy = 11$ cm. The interpolation is a simple nearest-neighbor scheme, chosen for efficiency and to maintain the binary nature of the data. The resulting binary video record $I(x, y, t)$ is tapered in time $t$ and space using a Bartlett window (Press et al. 1992) to reduce leakage, as well as to preferentially weight the breaking crests that are completely captured by the camera field of view.

The wavenumber–frequency spectrum is defined as

$$\mathcal{S}(k_x, k_y, f) = \iiint I(x, y, t) e^{-i2\pi k_x x} e^{-i2\pi k_y y} e^{-i2\pi f t} \, dx \, dy \, dt, \tag{4}$$

where $k_y$, $k_x$ are the wavenumbers ($m^{-1}$) approximately along and across the direction of wave breaking, respectively (see Fig. 1), and $f$ is the frequency (Hz). The spectrum $\mathcal{S}$ is normalized by bandwidths $dk_y$, $dk_x$, $df$, as well as the number of points in the double-sided, 3D transform. In practice, $\mathcal{S}$ is calculated for 23 quasi-independent windows (1024 frames each, 25% overlap) spanning each 30-min case study and then ensemble averaged to achieve approximately 46 degrees of freedom. The window lengths and grid resolution are chosen for efficiency, such that the dimensions of $I(x, y, t)$ are all $2^n$, where $n$ is any integer.

The short windows (102 s) are essential to isolate the motion of the breaking crests. Longer windows would result in whitened spectra from the episodic nature of the breaking (both in space and time). By choosing an appropriately short window length, the signal in $k_y$ is dominated by the distance a crest travels during breaking, and the signal in $f$ is dominated by the duration of a breaking event. Thus, the spectrum $\mathcal{S}(k_x, k_y, f)$ is not the wavenumber–frequency spectrum of the wave field, but rather it is the pixel-weighted signature of an average breaking event.

The 2D spectrum $\mathcal{S}(k_y, f) = \int \mathcal{S}(k_x, k_y, f) dk_x$ during moderate winds (8.5 m $s^{-1}$) is presented in Fig. 2a and shows a concentration of amplitude $S$ along a ridge in $k_y$, $f$ space. The spectral amplitude $S = \sqrt{\mathcal{S} \cdot \mathcal{S}^\star}$, where the star ($^\star$) indicates the complex conjugate, is related to the normalized number of whitecap pixels and is used instead of the more common spectral power $S^2$. There is a distinct $f$, $k_y$ slope related to the average movement of whitecaps through the camera field of view along the $y$ axis (e.g., the whitecap moving toward decreasing $y$ in Fig. 1). There is no slope observed in the other quadrants of $S(k_y, f)$ (not shown), because there is no significant movement toward increasing $y$. Likewise, there is no slope observed in the corresponding $S(k_x, f)$ (not shown), because there is no significant movement along the $x$ axis. Thus, analysis can be limited to a single

quadrant by the choice of camera orientation (along the principle axis of breaking-crest propagation). Here, the rectified images are aligned to the mean wind direction at 164°T, such that breaking crests propagated approximately along the $y$ axis. Analysis could be extended to other camera orientations by considering the componentwise contributions of slopes in other quadrants.

### c. *Speed transform*, $c = f/k_y$

Following the method of Chickadel et al. (2003), the change of variables

$$c = \frac{f}{k_y}, \tag{5}$$

defines the speed $c$ of signals moving along the $y$ axis in the video record. For directionally broad conditions, or cases with waves skewed relative to a chosen principle axis, the speed transform can be generalized to a vector $\mathbf{c} = f/\mathbf{k}$. To preserve amplitude spectral density, the Jacobian determinant $|df/dc| = |\mathbf{k}|$ accounts for changes in bandwidth (i.e., changes from square areas $dk_y\ df$ to curvilinear areas $dk_y\ dc$), such that

$$\int_{k_-}^{k_+}\int_{f_-}^{f_+} S(k_y, f)df\, dk_y = \int_{k_-}^{k_+}\int_{c(f_-)}^{c(f_+)} S(k_y, c)|k_y|dc\ dk_y. \tag{6}$$

The subscripts $\pm$ to the limits of integration denote the significant bands surrounding the peak in the wavenumber spectrum $S(k_y)$ and in the wavenumber–frequency spectra $S(k_y, f)$. Restricting to the bands around the peak is essential to prevent noise from biasing in the speed signal; the speeds captured are from $c(f_-)$ to $c(f_+)$ at each significant $k_y$. Several criteria for choosing significant bands are successful, such as using a fixed number of bands around the peak value (Bayly et al. 1994) or a priori estimates of noise level for band exclusion (Chickadel et al. 2003). Here, a practical approach is used, where bands exceeding 50% of the peak amplitude value (or 25% of peak power) are included as significant and all others are excluded.

Figure 2b shows the resulting $S(k_y, c)$ from the spectrum in Fig. 2a, where amplitude spectral density is concentrated in a quasi-normal distribution around 2 m s$^{-1}$ (consistent with time-domain estimates; see section 5a and Fig. 3 for comparison). The 1D speed spectrum is obtain by integrating over $k_y$ to obtain

$$S(c) = \int_{k_-}^{k_+} S(k_y, c)dk_y, \tag{7}$$

and we note that $S(c)$ is already an expected, or average, value that is normalized and tapered in both time and space. Physically, the speed spectrum $S(c)$ quantifies breaking crest speeds as weighted by leading edge pixels (i.e., length), including speed variations within individual breaking events (i.e., the evolution from onset to expiration of each crest). For directional cases, the scalar distribution of speed can be obtained componentwise as $S(c) = \sqrt{S(c_x)^2 + S(c_y)^2}$, and a spreading angle can be estimated by $\theta = 2\arctan[S(c_x) + S(c_y)]$.

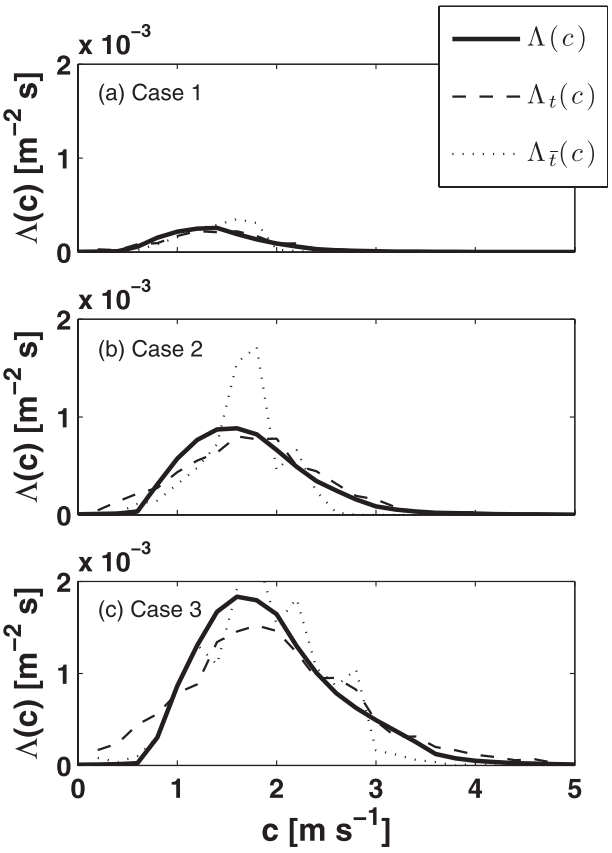


FIG. 3. The normalized distribution of total crest lengths as a function of speed during conditions with (a) low, (b) moderate, and (c) high wind speeds (see Table 1 for conditions corresponding to the case number in each panel). Methods compared are Fourier-based [$\Lambda(c)$, solid curves], time-domain average instantaneous [$\Lambda_t(c)$, dashed curves], and time-domain average characteristic [$\Lambda_{\bar{t}}(c)$, dotted curves]. The speed bandwidth is $dc = 0.2$ m s$^{-1}$.

### d. *Advection by dominant waves*

Short waves riding on the dominant waves are advected (i.e., Doppler shifted) by the orbital motion of the dominant waves. Correcting for the advection is important to avoid spurious high values in the speed distribution and accurately represent the small-scale breaking events. The appropriate advection speed $u_{\text{adv}}$ is different for each component (to avoid artificial

correction of the dominant waves), and can be estimated by (Gemmrich et al. 2008)

$$u_{\text{adv}} = \left(1 - \frac{c}{c_p}\right) u_{\text{orb}}, \tag{8}$$

where $u_{\text{orb}} = a(2\pi f_p)$ and $c_p = g^{-1}(2\pi f_p)$ are the wave orbital speed and deep-water phase speed, respectively, of the dominant propagating waves. The peak frequency $f_p$ and amplitude $a$ are obtained from the ultrasonic altimeter record of surface elevation (i.e., independent of the video data).

The true speed bands of the spectra are then

$$c = f/k_y\left(1 + \frac{u_{\text{orb}}}{c_p}\right) - u_{\text{orb}}, \tag{9}$$

and the amplitude spectral density $S$ is preserved. For locally generated wind seas, such as the data presented here, this correction is small, because breaking occurs on scales similar to the dominant waves. A similar correction can be made in the time domain; however, $u_{\text{adv}}$ is defined for each event as opposed to each component and is directly subtracted from the speed of the event (see section 4). Also, the Stokes drift $u_s = a^2(2\pi f)^3 g^{-1}$ can be removed in Eq. (9), but it is negligible for the data presented here.

### e. Crest length normalization

The speed spectrum $S(c)$ is rescaled by $L_{\text{total}}$ [Eq. (1)], which can be determined from the average number of leading edge pixels in $N$ binary images $\Sigma[I(x,y,t)]/N$ and the area normalized uniform pixel width $dx/A$ in the along-crest dimension. The spectrum contains total contribution of all crest lengths at each speed, and is directly related to the Phillips (1985) distribution by

$$\Lambda(c) = S(c)\frac{dx\sum I(x,y,t)}{NA\int S(c)dc}, \tag{10}$$

which is shown for each of the three case studies as the solid curves in Fig. 3. The examples are validated using distributions from two time-domain methods (see next section). The results are insensitive to changes in the criteria for selecting significant bands $f_{\pm}$, $k_{\pm}$.

We note that the final distribution is related to the commonly used ratio of whitecap coverage $W$ by the integral $W = dy\int\Lambda(c)dc$. We also note that statistics and related confidence intervals of the final distribution will follow a $\chi^2$ distribution with appropriate degrees of freedom (46 for the example presented).

## 4. Time-domain method

Here, a time-domain method adapted from Gemmrich et al. (2008) is described, and two variations are applied for comparison with the Fourier-based method. Tracking breaking crests in time is substantially slower (up to a factor of 10) computationally, despite beginning with the same initial steps (section 3a) to isolate the leading edges of crests and convert to binary signals $I(x_p, y_p, t)$. Centroid crest locations $Y(t) = [\Sigma y_p I(x_p, y_p, t)][\Sigma I(x_p, y_p, t)]^{-1}$ are determined for every frame, and the locations are used to estimate instantaneous (frame-to-frame) speeds $c(t) = [Y(t) - Y(t + dt)]dt^{-1}$ along the direction of crest propagation. Crest lengths $L(t)$ are also determined for each frame from the range of $x_p$ $I(x_p, y_p, t)$. (Multiple crests are tracked through shared frames by parsing the frames into subsections.) Advection is accounted for in the time domain by the direct subtraction of $u_{\text{adv}}$ [Eq. (8)] from each speed observation.

Subsets of $c(t)$, $L(t)$ can be averaged to single characteristic values $c(\bar{t})$, $L(\bar{t})$ for each breaking event, as in Gemmrich et al. (2008), to give

$$\Lambda_{\bar{t}}(c) = \frac{\sum_{c}^{c+dc} L(\bar{t})\tau}{AdcT}, \tag{11}$$

which is normalized by the duration of each event $\tau$ and of the entire record $T$. As such, using the characteristic values considers the contribution of each breaking event as a single component in the overall distribution of breaking waves. Alternatively, all of the instantaneous values can be averaged together to give

$$\Lambda_{t}(c) = \frac{\sum_{c}^{c+dc} L(t)}{AdcN}, \tag{12}$$

which is normalized by the number of frames $N$. Following Eq. (1), both distributions are normalized also by the imaged area $A$ and the speed bandwidth $dc$.

Geometrically, the characteristic values represent the area overturned during a breaking event as a rectangle $L(\bar{t})c(\bar{t})\tau$, while the instantaneous values represent the area overturned as an ellipsoid $\Sigma L(t)c(t)dt$ capturing the expansion and contraction of a breaking crest. The difference is in whether averaging is done for each crest and for the entire record, as in $\Lambda_{\bar{t}}(c)$, or just for the entire record, as in $\Lambda_t(c)$. Thus, $\Lambda_t(c)$ is the most natural comparison with the Fourier-based method, because it describes the contribution of each breaking event as many coupled components leading to the overall distribution of breaking waves.

## 5. Results

### a. Method comparison

In each of three cases, the new Fourier-based method is validated by two time-domain methods (Fig. 3). The distribution from averaging instantaneous speeds and lengths, $\Lambda_t(c)$ [Eq. (12)], produces the best agreement (Fig. 3, dashed curve), which is consistent with the interpretation of evolving crests that each contribute a subset to the overall distribution. The distributions from averaging characteristic speeds and lengths, $\Lambda_{\bar{t}}(c)$ [Eq. (11)], produce narrower, more jagged distributions (Fig. 3, dotted curves) that are biased by the discrete treatment of evolving crests. We note that $L_{\text{total}}$ [Eq. (1)] is constrained to be the same for all methods (i.e., the areas under the curves in Fig. 3) because the thresholding (section 3a) is the same for all methods.

For the time-domain results, the $\Lambda_t(c)$ values are biased high at low speeds ($c < 1$ in Fig. 3c) because the event-based advection correction adjusts all low instantaneous speeds $c(t)$, even if associated with the crests of long waves. This problem is avoided for $\Lambda_{\bar{t}}(c)$, because $u_{\text{adv}}$ goes to zero for long waves when using characteristic speeds $c(\bar{t})$ [Eq. (8)]. The frequency-based $\Lambda(c)$ also avoids this bias, because the advection correction goes to zero for waves at the peak of the power spectrum [Eq. (9)]. As further evidence, test runs without any advection correction give $\Lambda(c)$ and $\Lambda_t(c)$ distributions that are similar at all speeds (not shown). Thus, the Fourier-based $\Lambda(c)$ is the only distribution that both accurately corrects for advection [as does $\Lambda_{\bar{t}}(c)$] and completely represents the distribution of evolving crests [as does $\Lambda_t(c)$].

### b. Breaking rate

The area-normalized surface turnover rate is given by the first moment of the Phillips (1985) distribution,

$$R = \int c\Lambda(c)dc, \tag{13}$$

and is equivalent analytically to the frequency of breaking at a point. The frequency of breaking can be determined directly using the number of breaking pixels [Eq. (3)] in each case study,

$$f_{\text{brk}} = \frac{\sum\sum\sum I(x,y,t)}{MN\,dt}, \tag{14}$$

where $N$ is the number of images, $M$ is the total number of pixels in an image, and $dt$ is the time between sequential images (Jessup and Phadnis 2005). As further verification of the $\Lambda(c)$ methods, Fig. 4 shows agreement between the turnover rate $R$ and the frequency of breaking $f_{\text{brk}}$, as well as consistent values from the different methods. In addition, the breaking rates are within the range of previous results under similar conditions on Lake Washington (Weisman et al. 1984).

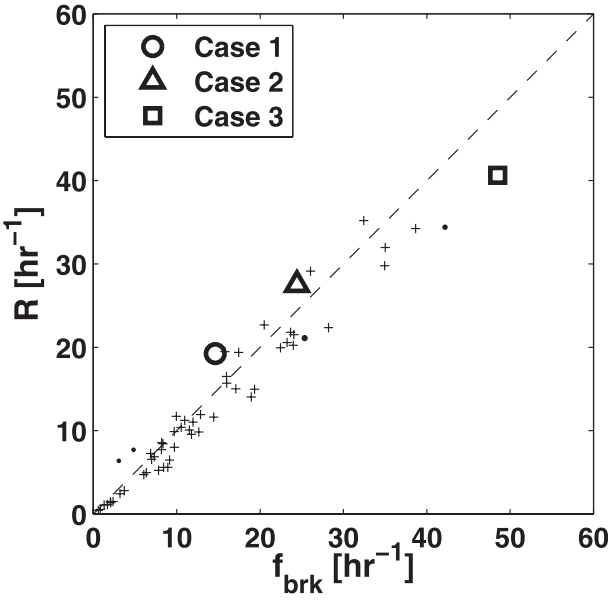


FIG. 4. Surface turnover rate vs direct frequency of breaking over a range of conditions. The rate from the Fourier-based $\Lambda(c)$ distribution is consistent with a direct count of the average amount of breaking at any given pixel. Rates from the time-domain $\Lambda_t(c)$ are similarly consistent (not shown). Symbols indicate the three case studies (circle, triangle, and square) described in Table 1. Additional data used in developing the method are shown from Lake Washington (dots) and Puget Sound (plusses) and reported in Thomson et al. (2009).

### c. Inferred energy dissipation

The spectral energy dissipation caused by wave breaking is given by (Phillips 1985; Duncan 1981)

$$\epsilon(c) = \frac{b\rho}{g} c^5 \Lambda(c), \tag{15}$$

where $\rho$ is density, $g$ is gravity, and $b$ is a scale parameter. Figure 5 shows $c^5\Lambda(c)$ for the three case studies versus a normalized speed $c/c_p$. Normalizing by the dominant phase speed $c_p$ shows the scale dependence of the dissipation and indicates that breaking at dominant scales is preferentially observed for shorter, smaller waves (Fig. 3, where wave height increases down the panels). As in previous studies, no evidence is found for a Kolmogorov-type energy cascade, but rather the mid-scale and larger events are found to dominate the dissipation (Gemmrich et al. 2008; Melville and Matusov 2002; Phillips et al. 2001). The presence of substantial

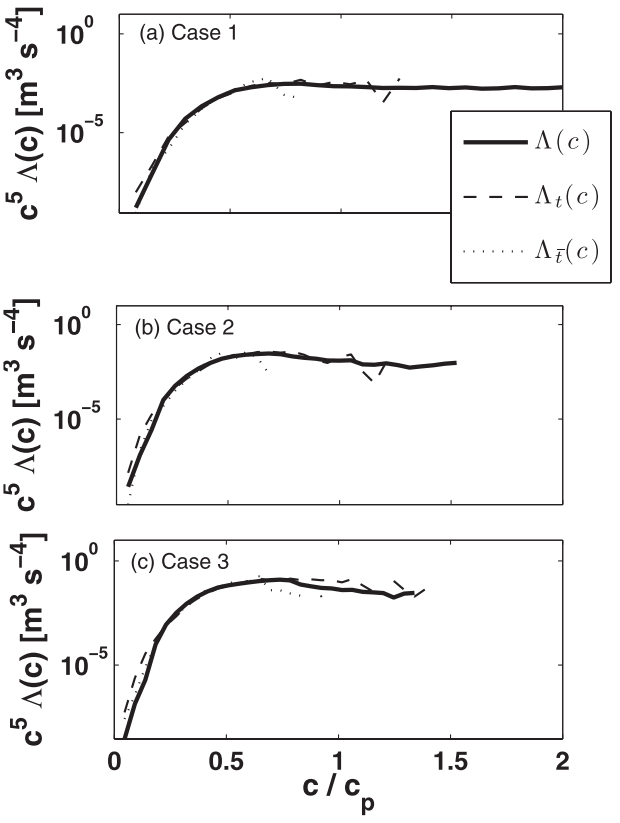


FIG. 5. Fifth moments of $\Lambda(c)$ vs normalized crest speed $c/c_p$, where $c_p$ is the peak phase speed of the background wave field, during conditions with (a) low, (b) moderate, and (c) high wind speeds (see Table 1 for conditions corresponding to the case number in each panel). Methods compared are Fourier-based [$\Lambda(c)$, solid curves], time-domain average instantaneous [$\Lambda_t(c)$, dashed curves], and time-domain average characteristic [$\Lambda_{\bar{t}}(c)$, dotted curves]. The fifth moment is related to the energy dissipation by an undetermined physical constant $b$ [Eq. (15)].

dissipation at speeds $c/c_p \gg 1$ differs from previous results, and may be owing to a rapidly growing field of young waves. Comparison with in situ observations of turbulent dissipation suggests that $b$ is of order $10^{-2}$ (Thomson et al. 2009).

## 6. Discussion

While the Fourier-based method to calculate the speed distribution of total breaking crest lengths $\Lambda(c)$ is shown to be consistent with time-domain methods, physical interpretation remains to be established. The best agreement is found between the Fourier-based method and a time-domain approach that includes instantaneous fluctuations of crest speeds and lengths. The approach differs somewhat from the conventional use of single values per breaking crest, and is suggested as more rigorous approach that is robust to sparse observations, such as during intermittent breaking.

In the original scaling argument for energy dissipation as the fifth moment of speed and length [Eq. (15)], Duncan (1981) considered discrete breaking waves in a laboratory experiment. A single, deterministic speed and length for each breaking wave is straightforward to evaluate in a laboratory context. Extending to field measurements, however, requires a stochastic treatment to capture the uncertainty and the bandwidth of crest speeds and lengths. Even under the best measurement conditions, natural breaking waves do not have uniquely determined quantities. A breaking event can last up to several seconds, during which the crest (and related dissipation) evolves in strength and extent. Thus, single values overly discretize the breaking process. Using multiple components provides the most complete description of each breaking event (and related evolution). The subsequent ensemble averaging of all components produces reliable statistics and smooth $\Lambda(c)$ distributions (e.g., Fig. 3).

In a spectral context, this implies that individual breaking events dissipate energy at multiple scales. This implication is heuristically consistent with the treatment of depth-limited (surf zone) breaking, in which individual waves oversteepen and break as the superposition of many coupled harmonic components that transfer energy across scales (Herbers et al. 2000). Alternatively, one could interpret the use of multiple speed components as indicative of a changing dispersion relation or a changing ratio of crest-to-linear speed during breaking. In either interpretation, the underlying idea is that wave breaking is not a steady process, and thus instantaneous fluctuations are important for determining the bulk dissipation.

## 7. Conclusions

A Fourier-based method to determine the speed distribution of breaking crest lengths $\Lambda(c)$ is shown to agree with time-domain methods, while having advantages in efficiency and physical interpretation. The methods are compared using video observations of fetch-limited breaking waves on Lake Washington, Washington, during a range of conditions. Estimates of $\Lambda(c)$ are quasi-normal distributions with maxima at speeds somewhat less than the dominant phase speed, consistent with previous work. Breaking rates are well matched with independent estimates, and energy dissipation is dominated by larger scale events. A bias toward visible breakers (whitecaps) is present, and field adaptation of laboratory infrared techniques (Jessup and Phadnis 2005) to evaluate small scales (microbreakers) is needed.

*Acknowledgments.* Thanks to J. Gemmrich (U. Victoria) and C. Chickadel (APL-UW) for discussions and insights during method development. Thanks to P. J. Rusello, E. Boget, and the APL-UW Marine Department for efforts and support during data collection. Thanks to Bill Evans and the Kenmore Parks Department for use of the pier at Log Boom Park. Funding provided by the National Science Foundation Grant OCE 0549780 and the Office of Naval Research Grant N000140610809.

## REFERENCES

Banner, M. L., and D. H. Peregrine, 1993: Wave breaking in deep water. *Annu. Rev. Fluid Mech.,* **25,** 373–397.

——, and W. L. Pierson, 2007: Wave breaking onset and strength for two-dimensional deep water wave groups. *J. Fluid Mech.,* **585,** 93–115.

——, A. V. Babanin, and I. Young, 2000: Breaking probability for dominant waves on the sea surface. *J. Phys. Oceanogr.,* **30,** 3145–3160.

Bayly, P. V., R. E. Hillsley, R. J. Gerstle, P. D. Wolf, W. M. Smith, and R. E. Ideker, 1994: Estimation of propagation speed during ventricular fibrillation from frequency-wavenumber power spectra. *Proc. Computers in Cardiology 1994,* Bethesda, MD, IEEE, 161–164.

Chickadel, C. C., R. A. Holman, and M. H. Freilich, 2003: An optical technique for the measurement of longshore currents. *J. Geophys. Res.,* **108C,** 3364, doi:10.1029/2003JC001774.

Duncan, J. H., 1981: An experimental investigation of breaking waves produced by a towed hydrofoil. *Proc. Roy. Soc. London,* **A377,** 331–348.

Gemmrich, J. R., and D. Farmer, 1999: Observations of the scale and occurrence of breaking surface waves. *J. Phys. Oceanogr.,* **29,** 2595–2606.

——, and ——, 2004: Near-surface turbulence in the presence of breaking waves. *J. Phys. Oceanogr.,* **34,** 1067–1086.

——, M. L. Banner, and C. Garrett, 2008: Spectrally resolved energy dissipation rate and momentum flux of breaking waves. *J. Phys. Oceanogr.,* **38,** 1296–1312.

Herbers, T. H. C., N. R. Russnogle, and S. Elgar, 2000: Spectral energy balance of breaking waves within the surf zone. *J. Phys. Oceanogr.,* **30,** 2723–2737.

Holland, K. T., R. A. Holman, T. C. Lippmann, J. Stanley, and N. Plant, 1997: Practical use of video imagery in nearshore oceanographic field studies. *IEEE J. Ocean. Eng.,* **22,** doi:10.1109/48.557542.

Jessup, A., and K. Phadnis, 2005: Measurement of the geometric and kinematic properties of microscale breaking waves from infrared imagery using a PIV algorithm. *Meas. Sci. Technol.,* **16,** 1961–1969.

Melville, W. K., 1996: The role of surface-wave breaking in air-sea interaction. *Annu. Rev. Fluid Mech.,* **28,** 279–321.

——, and R. J. Rapp, 1985: Momentum flux in breaking waves. *Nature,* **317,** 514–516.

——, and P. Matusov, 2002: Distribution of breaking waves at the ocean surface. *Nature,* **417,** 58–63.

Phillips, O. M., 1985: Spectral and statistical properties of the equilibrium range in wind-generated gravity waves. *J. Fluid Mech.,* **156,** 495–531.

——, F. Posner, and J. Hansen, 2001: High range resolution radar measurements of the speed distribution of breaking events in wind-generated ocean waves: Surface impulse and wave energy dissipation rates. *J. Phys. Oceanogr.,* **31,** 450–460.

Press, H. W., S. A. Teukolsky, W. T. Vetterling, and B. P. Flannery, 1992: Numerical recipes. *The Art of Scientific Computing,* 2d ed. Cambridge University Press, 657–658.

Rapp, R. J., and W. K. Melville, 1990: Laboratory measurements of deep-water breaking waves. *Philos. Trans. Roy. Soc. London,* **331A,** 735–800.

Thomson, J., J. R. Gemmrich, and A. T. Jessup, 2009: Energy dissipation and the spectral distribution of whitecaps. *Geophys. Res. Lett.,* **36,** L11601, doi:10.1029/2009GL038201.

Weisman, M. A., S. S. Atakturk, and K. B. Katsaros, 1984: Detection of breaking events in a wind-generated wave field. *J. Phys. Oceanogr.,* **14,** 1608–1619.